Model for the Patterns of Salt-Spray-Induced Chloride Corrosion in Concretes under Coupling Action of Cyclic Loading and Salt Spray Corrosion

Authors:

Ruixue Liu, Huiguang Yin, Lianying Zhang, Bing Li, Xianbiao Mao

Abstract:

In this study, the patterns of chloride ion erosion of unsaturated concrete subjected to the coupling action of cyclic loading and salt spray corrosion were experimentally studied, and Fick's Second Law was used to fit the variation patterns of chloride concentration to obtain the chloride diffusion coefficient. Accordingly, we have established a mathematical model that describes chloride transport in unsaturated concrete and accounts for the effects of gas flow, water migration, convection diffusion, and capillary action. This model is composed of three equations—the gas flow equation, the solution flow equation, and the solute convection?diffusion equation. The COMSOL numerical analysis software was subsequently used to obtain solutions for this model, based on parameters such as porosity and the chloride diffusion coefficient. Subsequently, the saturation, relative permeability, and the chloride ion concentration during the first corrosion cycle were analyzed. The numerical results were consistent with the experimental values and were therefore superior to the values obtained using Fick's Second Law.

Record Type: Published Article

Submitted To: LAPSE (Living Archive for Process Systems Engineering)

Model for the Patterns of Salt-Spray-Induced Chloride Corrosion in Concretes under Coupling Action of Cyclic Loading and Salt Spray Corrosion

Ruixue Liu [1,2], Huiguang Yin [2], Lianying Zhang [2], Bing Li [2] and Xianbiao Mao [1,*]

[1] State Key Laboratory for Geomechanics & Deep Underground Engineering, China University of Mining and Technology, Xuzhou 221116, China; ruixue1964@163.com

[2] School of Civil Engineering, Xuzhou Institute of Technology, Xuzhou 221008, China; yhg@xzit.edu.cn (H.Y.); zhanglianying@126.com (L.Z.); Libing_libing_2007@163.com (B.L.)

* Correspondence: xbmaocumt@163.com; Tel.: +86-151-6218-3074

check for updates

Abstract: In this study, the patterns of chloride ion erosion of unsaturated concrete subjected to the coupling action of cyclic loading and salt spray corrosion were experimentally studied, and Fick's Second Law was used to fit the variation patterns of chloride concentration to obtain the chloride diffusion coefficient. Accordingly, we have established a mathematical model that describes chloride transport in unsaturated concrete and accounts for the effects of gas flow, water migration, convection diffusion, and capillary action. This model is composed of three equations—the gas flow equation, the solution flow equation, and the solute convection–diffusion equation. The COMSOL numerical analysis software was subsequently used to obtain solutions for this model, based on parameters such as porosity and the chloride diffusion coefficient. Subsequently, the saturation, relative permeability, and the chloride ion concentration during the first corrosion cycle were analyzed. The numerical results were consistent with the experimental values and were therefore superior to the values obtained using Fick's Second Law.

Keywords: Unsaturation; chloride; concrete; coupling model; numerical calculation

1. Introduction

Concrete structures in tidal zones (or splash zones) are prone to damage owing to various physical, chemical, and biological factors [1–4]. One of the main causes of damage in reinforced concrete structures is chloride intrusion, which usually leads to steel-bar corrosion and concrete cracks [5,6]. There have been many studies on the pattern and mechanism of chloride intrusion in tidal zones (or splash zones). Most of these studies have focused on the transport of chloride in unsaturated concrete. It is generally accepted that chloride intrusion in a tidal or splash zone primarily occurs via capillary adsorption on the concrete surface and diffusion within the concrete [7–9]. Based on Fick's Second Law, Jin et al. studied the effects of water on chloride intrusion and established a convection–diffusion model for chlorides in unsaturated concrete [7]. Pan et al. established a convection–diffusion equation for chlorides and obtained solutions for this equation, based on the theoretical understanding that the transport processes of chlorides in unsaturated concrete are jointly determined by diffusion and convection effects [10]. Using dual-porosity models, Yan et al. established equations that describe the transport of chlorides in concrete and the fractures owing to the coupling of concentration gradients and pore-fluid saturation gradients [11]. Li et al. proposed a model for chloride transport based on water transport mechanisms on concrete surfaces that are alternatingly wet and dry, and they experimentally validated this model [12,13]. Polder studied chloride transport patterns (in wet–dry cycles) in unsaturated concrete using an electrochemically accelerated experimental approach [14].

Several scholars have also constructed water–chloride transport models based on the effects of water migration in concrete pores [15–18]. For example, Zanden et al. adopted the diffusion coefficient to describe the water transport processes in concrete, and they established the transport equations for water and chlorides in concrete samples subjected to wet–dry cycles using the convection–diffusion model [19].

Currently, most studies on the patterns of chloride transport in unsaturated concrete are based on Fick's Second Law; these studies comprehensively account for the effects of capillary action, convection–diffusion, and water migration [20–22]. However, the transmission of chlorides in unsaturated concrete is an extremely complex process and is influenced by a variety of factors. In actual systems, gas flow is also an important factor for the transport of chlorides. Therefore, the objective of this study was to establish a chloride transport model that accounts for the effects of gas flow, water migration, capillary action, and convection–diffusion. The COMSOL numerical analysis program was used to obtain solutions for this model. The results were compared with experimental data to validate the model.

2. Experimental Research on Chloride Transport in Concrete

2.1. Materials

The cementitious materials used in the experiment were Portland cement, mineral powder (G), and fly ash (F) that were supplied by two local companies. The fine aggregate was river sand with a fineness modulus of 2.8 and an apparent density of 2769 kg/m^3. The coarse aggregate was crushed limestone with a size of 5–20 mm and an apparent density of 2719 kg/m^3. The slushing agent for the concrete was carboxylic acid provided by Wulong, and the mix proportion of the concrete is summarized in Table 1.

Table 1. Mix ratio of concrete.

Water–Cement Ratio	Admixture	Content (%)	Cement (kg/m^3)	Fly Ash (kg/m^3)	Mineral Powder (kg/m^3)	Sand (kg/m^3)	Stone (kg/m^3)	Water (kg/m^3)
0.32	F + G	15 + 35	226	68	158	740	1112	145

The specimens were kept in molds for about 24 h at room temperature (20 $\pm$ 5 °C) after casting. Then, they were remolded and placed in a standard curing room of a controlled temperature (20 $\pm$ 2 °C) and a relative humidity of more than 95% for 28 days before they were tested.

2.2. Test Methods

The dimensions of the concrete samples were 100 $\times$ 100 $\times$ 400 mm. The serial numbers and quantity of the samples are shown in Table 2, whereas Figure 1 shows the flowchart of the tests. The experimental procedures are described below:

1. Uniaxial compression tests were performed on the concrete samples that had been cured for 28 days to measure their strength (σ_c).
2. Three cyclic loading protocols (i.e., 50%, 65%, and 80% σ_c) were used to obtain concrete samples with three different porosities and were numbered as #1, #2, and #3, respectively. The detailed experimental steps of applying the cyclic loads are as follows: firstly, each specimen was loaded at the loading rate of 5 kN/s using force control, until the load reached the specified load setting value (here, the set value was 50%, 65%, or 80% of the compressive strength limit (c)), and then the load was maintained for 120 s. After that, each specimen was unloaded at the unloading rate of 5 kN/s, until the load value was 0 kN, and then the completely unloaded state was maintained for 120 s. This procedure was repeated for 5 cycles in total, according to the above loading and unloading operations. Finally, the sample was completely unloaded (load was 0 kN).

3.　After cyclic loading, the samples with different porosities were placed in a drying oven and dried at 40 °C for 48 h. Subsequently, the samples were weighed, and the initial weights were recorded. Subsequently, the samples were soaked in water for 48 h. The weights of the samples at saturation were measured, and their porosities were calculated (Table 3).

4.　One of the 100 × 400 mm surfaces of the samples was used as the corrosion surface, whereas the other sides were sealed using epoxy resins. Subsequently, the concrete samples were placed in an artificial marine climate simulation laboratory for salt spray corrosion tests. The relative humidity was 75–80%, and the duration of the salt spray was 12 h, after which the samples were dried for another 12 h—this cycle was continuously repeated for the duration of the test. The concentration of the NaCl solution used in this test was 5%.

5.　When the corrosion time reached 30, 110, 190, and 270 days, concrete powders were obtained from the samples at depths of 5, 10, 15, 20, 25, 30, 35, and 40 mm, which were sealed in plastic bags. Subsequently, 4 g of the concrete powder was mixed with 40 g of distilled water in a reagent bottle. The bottle was shaken for 30 min in a solution shaker before being allowed to settle for 24 h.

6.　The concentration of the chloride ions was measured using a DY-2501A Chloride Meter.

7.　After testing, the holes in the concrete samples were filled with silicon sealant, and the samples were returned to the laboratory for further corrosion until the subsequent time point, and subsequently, step (6) was repeated. This was continued until the end of the experiment.
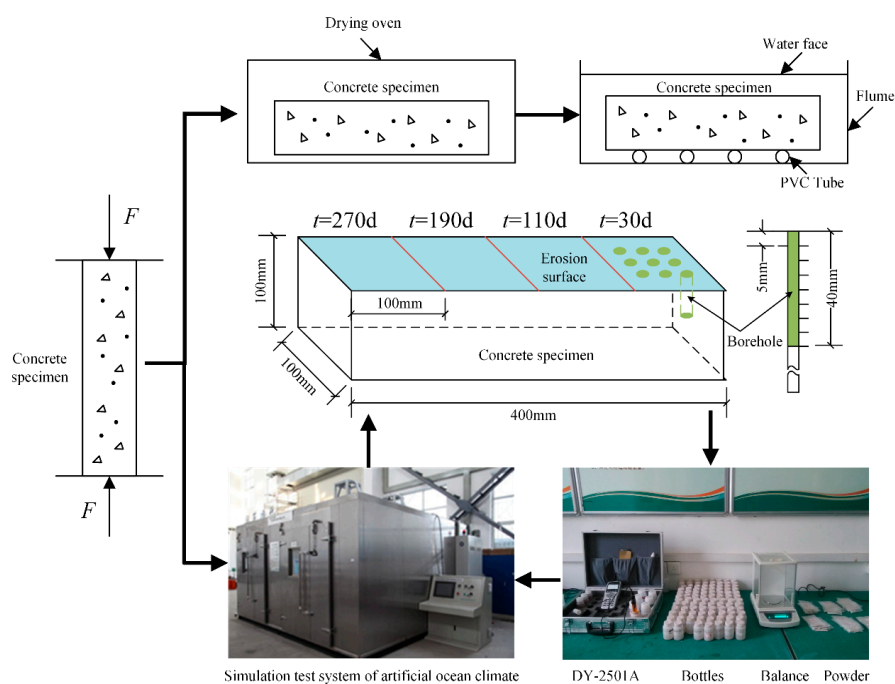

Figure 1. Flow chart of the test.

Table 2. Number of specimens.

Sample NO.	1#	2#	3#
NO./piece	3	3	3

Table 3. Porosity of concrete.

Sample NO.	Porosity ϕ (%)			
	Sample 1	Sample 2	Sample 3	Mean
1	3.92	3.22	3.30	3.49
2	3.90	4.21	3.38	3.83
3	4.73	4.13	5.26	4.71

2.3. Results and Discussion

Figure 2 shows the variational curve of *c* against *l* in the concrete samples (*c* is the concentration of chloride ions in the concrete samples, and *l* is the depth from the specimen surface). Figure 2a–d correspond to the time points at 30, 110, 190, and 270 days, respectively. It was observed that *c* decreased with an increase in *l*. When *l* < 15 mm, *c* decreased rapidly, with an average decrease of 80.80%; when *l* > 15 mm, *c* decreased slowly, and the average decrease was only 39.10%. As stated previously, cyclic salt sprays were used as the mechanism of corrosion in this study. The intrusion of chloride ions was mainly driven by capillary actions and concentration gradients. Since the surface of the concrete was the first area that came into contact with the external chlorides, large quantities of chloride accumulated on the surface, resulting in a large chloride concentration gradient. By comparison, fewer chloride ions accumulated deep inside the concrete samples, and, consequently, the chloride ion concentrations were relatively small. It was also observed that, for the same *l*, *c* increased with an increase in the porosity; this is because a high porosity increases water and gas permeability, which promotes chloride accumulation.

(a) 30 days

(b) 110 days

(c) 190 days

(d) 270 days
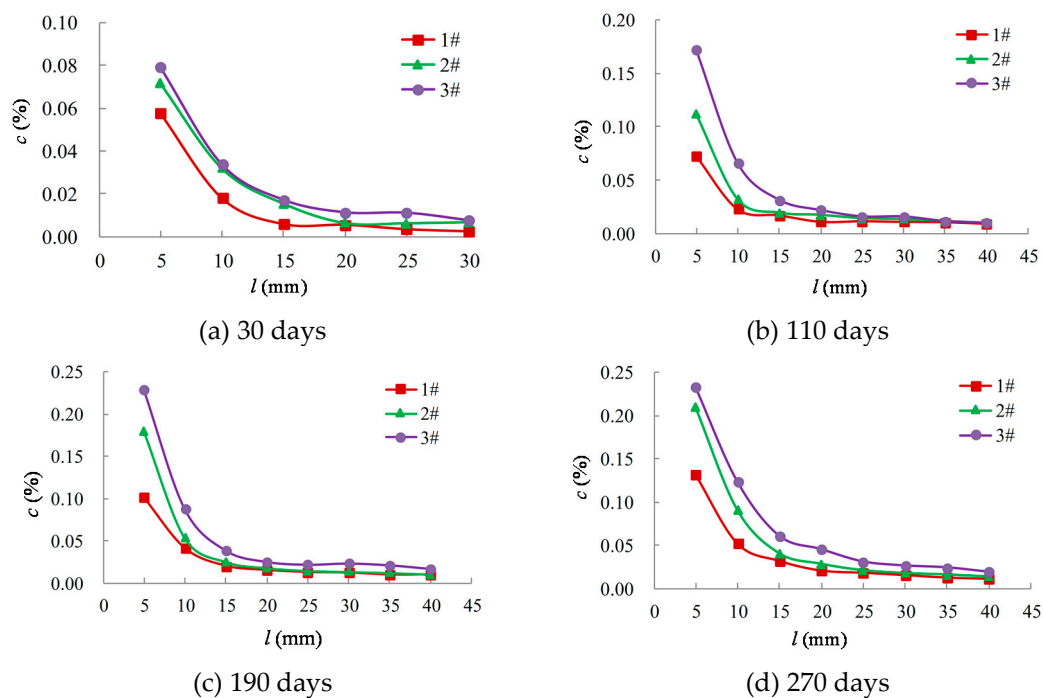
Figure 2. The change curves of chloride ion concentration, *c*, with depth, *l*.

Fick's Second Law was used to fit the pattern of chloride corrosion.
Fick's Second Law is expressed as

$$C(l,t) = C_0 + (C_s - C_0)(1 - erf\frac{l}{2\sqrt{Dt}})$$

(1)

where C_0 denotes the initial mass concentration of chloride in an arbitrary section of the concrete, C_s is the mass concentration of chloride ions on the concrete surface at an arbitrary time (t), D denotes the diffusion coefficient of chloride ions, t represents time, l represents the depth, and *erf* represents the error function.

By re-arranging Equation (1), the diffusion coefficient of chloride ions can be calculated by

$$D = \frac{1}{t}\left\{ l/2erf^{-}\left[1 - \frac{C(l,t) - C_0}{C_s - C_0} \right] \right\}^2 \tag{2}$$

where C_s is calculated as follows:

$$c_s = \frac{\phi \rho_w \omega}{\rho_s + \phi \rho_w \omega} \times \frac{35.5}{58.5} \times 100\% \tag{3}$$

where ϕ denotes the concrete porosity, ρ_w is the density of the NaCl solution, ρ_s is the concrete density, and ω is the mass percentage of NaCl in the solution. Further, ϕ assumed the values of the average porosities in Table 3, which were 3.49%, 3.83%, and 4.71%, ρ_s was 2420.67 kg/m³, ρ_w was 1050 g/m³, and ω was 5%.

The diffusion coefficient of the chlorides when l = 5 mm was calculated using MATLAB with Equation (3) (Table 4). The average value was used in the subsequent numerical calculations.

Table 4. Chloride diffusion coefficient, D.

Sample NO.	Chloride Diffusion Coefficient (D) ($\times 10^{-12}$ m²/s)				
	t = 30 d	t = 110 d	t = 190 d	t = 270 d	Mean
1	5.243	1.592	1.126	0.979	2.235
2	5.804	2.089	2.046	1.957	2.974
3	6.123	3.314	3.066	2.667	3.793

3. Model for Coupled Water–Gas–Chloride Transport

3.1. Basic Assumption

The model for coupled water–gas–chloride transport in unsaturated concrete was established with the following assumptions: (a) concrete is a single porosity medium, (b) the liquids and gases in concrete are ideal liquids and gases, (c) the influence of temperature on parameters such as dynamic viscosity is negligible, (d) only the transmission of a single solute (chloride ions) in concrete is considered, (e) in unsaturated concrete, the liquid phase is the chloride solution, whereas the gas phase is air, (f) there is no exchange of matter between the gas and the liquid phases over the entirety of the process, and (g) it is assumed that the solute (chloride ions) does not evaporate throughout the process, i.e., there is no exchange of matter between the gas phase and the solute [23–26].

In this paper, the gas–liquid two-phase flow model in a single-porosity medium was deduced first, and then the diffusion and gas–liquid two-phase flow were linked using the mass continuous equation according to the relationship between the saturation and the diffusion model.

3.2. Gas Flow Model

The equation of the continuity of gaseous masses without considering the source term is as follows:

$$\frac{\partial m_g}{\partial t} + \nabla \cdot \left(\rho_g \vec{q_g} \right) = 0 \tag{4}$$

where m_g denotes the mass of air, ρ_g is the air density, and $\vec{q_g}$ is the Darcy velocity vector.

In the following subsection, explanations are provided for each of the terms in Equation (4).

(1) Expression of the Gaseous Mass

The gaseous mass is expressed as

$$m_g = \rho_g \phi (1 - S_w) \tag{5}$$

where ϕ denotes the porosity of concrete and S_w is the water saturation.

According to the state equation of ideal gases, $\rho_g = \frac{M_g}{RT} P_g$, where M_g denotes the molecular mass of the gas, R is the gas constant, and T is the absolute temperature, Equation (5) can be written as

$$m_g = \frac{M_g}{RT} P_g \phi (1 - S_w) \tag{6}$$

(2) Equation of Porosity

When subjected to small loads or no load, the deformations in the porous media are mainly driven by pore pressure; hence, pore deformation occurs without significant changes in the particle volume.

In order to facilitate subsequent derivations, α was introduced to represent the pore deformation caused by changes in pore pressure:

$$\alpha = \frac{1}{U_w} \frac{dU_w}{dP} \tag{7}$$

where U_w denotes the volume of the pores. Thus, porosity may be expressed by

$$\phi = \frac{f(P)}{1 + f(P)} \tag{8}$$

where $f(P) = \frac{\phi_0}{1+\phi_0} e^{\alpha(P-P_0)}$, ϕ_0 is the initial porosity, and P_0 is the initial pore pressure.

(3) Darcy Velocity Vector of the Gas Phase

Darcy's law in the gas phase for a unit volume of porous concrete can be expressed as

$$\vec{q_g} = -\frac{k_{ge}}{\mu_g} \nabla P_g \tag{9}$$

where k_{ge} is the effective permeability of the gas phase (phase permeability) and μ_g is the dynamic viscosity of the gas phase.

(4) Expression for Effective Permeability

The expression for effective permeability is

$$k_{ge} = k_{rg} \cdot k \tag{10}$$

where k_{rg} is the relative permeability of the gas phase and k is the absolute permeability of the porous concrete.

(5) Expression for Absolute Permeability

Absolute permeability is the permeability when only one fluid (single phase) exists in the pores of the concrete, the fluid does not react with the concrete, and the fluid flows in accordance with the Darcy linear percolation law.

Absolute permeability is an important parameter for characterizing porous media, since it is closely related to the porosity of the medium. In this study, the relationship between the permeability and porosity in porous media, as reported by Chilingar, was defined as [27]

$$k = \frac{d^2 \phi^3}{72(1 - \phi^2)} \tag{11}$$

where k denotes the permeability of porous media, ϕ is the porosity of porous media, and d is the effective diameter of the particles in porous media. Based on Equation (8), the following equation was obtained:

$$k = k_0 \frac{(1 - \phi_0)^2}{\phi_0{}^3} \frac{f(P)^3}{1 - f(P)} \tag{12}$$

(6) Saturation and Relative Permeability

Fluid saturation is defined as the ratio of the volume of a fluid in a pore of an object to the pore volume, expressed as a percentage or fraction.

Based on the theories related to oil reservoir models [15], the relationship between the relative permeability, water pressure, gas pressure, and saturation [28,29] is derived in the following.

The capillary pressure is expressed as

$$P_c = P_e(S_w^*)^{-\frac{1}{\lambda}} = P_g - P_w \tag{13}$$

where P_e denotes the constant capillary pressure at the entrance, S_w^* is the saturation of the standard liquid phase, and λ is the pore size distribution index.

The relative permeability is expressed as

$$k_{rw} = (S_w^*)^{\frac{2+3\lambda}{\lambda}} \tag{14}$$

$$k_{rg} = (1 - S_w^*)^2 [1 - (S_w^*)^{\frac{2+\lambda}{\lambda}}] \tag{15}$$

The relationship between the standard liquid phase saturation and water–gas saturations is expressed as

$$S_w^* = \frac{S_w - S_{wr}}{1 - S_{gr} - S_{wr}} \tag{16}$$

$$S_w + S_g = 1 \tag{17}$$

where S_{wr} and S_{gr} are relevant constants.

By re-arranging Equation (13), we obtain

$$S_w^* = \left(\frac{P_e}{P_g - P_w} \right)^\lambda \tag{18}$$

By substituting Equation (18) into Equations (14) and (15), the relationships between the relative permeability, water pressure, and gas pressure are derived as

$$k_{rw} = \left(\frac{P_e}{P_g - P_w} \right)^{2+3\lambda} \tag{19}$$

$$k_{rg} = \left[1 - \left(\frac{P_e}{P_g - P_w} \right)^\lambda \right]^2 \left[1 - \left(\frac{P_e}{P_g - P_w} \right)^{2+\lambda} \right] \tag{20}$$

The relationship between saturation, water pressure, and gas pressure can be obtained by rearranging Equation (16):

$$S_w = (1 - S_{gr} - S_{wr}) \left(\frac{P_e}{P_g - P_w} \right)^\lambda + S_{wr} \tag{21}$$

(7) Flow Model for the Gaseous Phase

By substituting Equations (6), (8), (9), and (19)–(21) into Equation (4), the flow model for the gaseous phase can be obtained as

$$\left[\phi(1-S_w)\left[1+\frac{\alpha P_g}{1+f(P_g)}\right]+\phi P_g \lambda \left(1-S_{gr}-S_{wr}\right)\frac{P_e^\lambda}{\left(P_g-P_w\right)^{(1+\lambda)}} \right]\cdot\frac{\partial P_g}{\partial t}$$
$$-\left[\phi P_g \lambda \left(1-S_{gr}-S_{wr}\right)\frac{P_e^\lambda}{\left(P_g-P_w\right)^{(1+\lambda)}} \right]\cdot\frac{\partial P_w}{\partial t}+\nabla\cdot\left(-\frac{k_{rg}k}{\mu_g}P_g\nabla P_g\right)=0 \tag{22}$$

3.3. Flow Model for the Liquid Phase

(1) Continuity Equation of Liquid Masses

The continuity equation of liquid masses is expressed as

$$\frac{\partial m_w}{\partial t}+\nabla\cdot(\rho_w \vec{q_w})=0 \tag{23}$$

where m_w denotes the mass of the solution in a unit volume of porous concrete, ρ_w is the density of the solution, and $\vec{q_w}$ refers to the Darcy velocity vector of the solution.

(2) Mass of the Liquid Phase

The mass of the liquid phase is expressed as

$$m_w=\rho_w \phi S_w \tag{24}$$

where ρ_w is the density of the solution, ϕ is the porosity, and S_w is the saturation of the solution.

During chloride transport in concrete, the pore pressure and the solution concentration change, which leads to changes in the solution density. Therefore, ρ_w is a function of P and c:

$$\rho_w=\rho_w(P,c) \tag{25}$$

In order to characterize the variation of density with the pore pressure and the solution concentration, we introduced a compressible pressure coefficient, β_p, and a compressible concentration coefficient, β_c:

$$\beta_P=\frac{1}{\rho_w}\frac{d\rho_w}{dP}$$
$$\beta_c=\frac{1}{\rho_w}\frac{d\rho_w}{dc} \tag{26}$$

where β_p denotes the ratio between the change in density caused by the unit pressure changes and the initial density, whereas β_c denotes the ratio between the density changes caused by the changes in the unit concentration and the initial density.

Subsequently, the relationship between the variations in solution density with the pore pressure and the solution concentration can be obtained as follows:

$$\rho_w=\rho_{w0}e^{[\beta_P(P-P_0)+\beta_c(c-c_0)]} \tag{27}$$

where ρ_{w0} denotes the initial solution density, P_0 is the initial pore pressure, and c_0 is the initial concentration of the chloride ions.

(3) Darcy Velocity Vector of the Liquid Phase

Darcy's law for the liquid phase in a unit volume of porous concrete can be expressed as

$$\vec{q_w}=-\frac{k_{we}}{\mu_w}\nabla P_w \tag{28}$$

where k_{we} denotes the effective permeability of the liquid phase (phase permeability) and μ_w is the dynamic viscosity of the liquid phase.

The effective permeability can be expressed as

$$k_{we} = k_{rw} \cdot k \tag{29}$$

where k_{rw} denotes the relative permeability of the liquid phase and k is the absolute permeability of the porous concrete media. Therefore, we obtain

$$\overrightarrow{q_w} = -\frac{k_{rw} \cdot k}{\mu_w} \nabla Pw \tag{30}$$

(4) Flow Model for the Liquid Phase

The flow model of the liquid phase is

$$
-\nabla \cdot \left(\frac{\rho_w k_{rw} k}{\mu_w} \nabla P_w \right) - \left[\lambda \left(1 - S_{gr} - S_{wr} \right) \frac{\rho_w \phi P_e^\lambda}{\left(P_g - P_w \right)^{(1+\lambda)}} \right] \frac{\partial P_g}{\partial t}
$$
$$
+ \left\{ \rho_w \phi S_w (\beta_P + \beta_c) + \frac{S_w \rho_w \alpha \phi}{1 + f(P_w)} + \left[\lambda \left(1 - S_{gr} - S_{wr} \right) \frac{\rho_w \phi P_e^\lambda}{\left(P_g - P_w \right)^{(1+\lambda)}} \right] \right\} \frac{\partial P_w}{\partial t} + \left[\rho_w \phi_0 (\beta_P + \beta_c) \right] \frac{\partial c}{\partial t} \tag{31}
$$

3.4. Convection–Diffusion Models for Chlorides

The transport of chlorides in concrete is a complex process, and it may be treated as the transport of solutes (chlorides) in solution. Solute transport in porous media is influenced by various factors, such as convection, molecular diffusion, mechanical dispersion, precipitation–dissolution combined effects, and chemical adsorption. In this study, only convection, mechanical dispersion, and chemical adsorption were considered in the convection–diffusion model for chlorides in unsaturated concrete.

When the concrete pores are filled with the solution, the pore water inside the concrete does not migrate as a whole. Under the condition that the chloride ion and the hydration product of the concrete do not react chemically, the process of chloride ions migrating from the outside of the concrete to the interior of the concrete, depending on the concentration gradient difference inside and outside of the concrete, can be considered as a pure diffusion process. Convection refers to the phenomenon of the whole substance migrating with a carrier solution. The main cause of the convection of chloride ions in concrete is the directional seepage of the pore liquid under pressure, capillary adsorption, and electric field forces [30].

Accordingly, S_w was introduced into the continuity equation for the mass of chlorides in saturated concrete, from which the continuity equation for chloride masses in unsaturated porous media was obtained as follows:

$$\frac{\partial(m_c)}{\partial t} - \nabla \cdot (S_w \phi D \cdot \nabla c) + \nabla \cdot (\overrightarrow{v} c) = 0 \tag{32}$$

where the mass of chloride ions in the solution is expressed as $m_c = S_w \phi c - (1 - \phi) \rho_s K_L \frac{C_{max} c}{1 + K_L c}$ and $\overrightarrow{v_w}$ is the Darcy velocity vector of the solution.

By substituting the relevant equations into Equation (32), the convection–dispersion model for chlorides in unsaturated concrete was obtained as follows:

$$
- \left[\left(1 - S_{gr} - S_{wr} \right) \frac{\phi c \lambda P_e^\lambda}{\left(P_g - P_w \right)^{(1+\lambda)}} \right] \frac{\partial P_g}{\partial t} + \left[\left(c + \rho_s K_L \frac{C_{max} c}{1 + K_L c} \right) \frac{S_w \alpha \phi}{1 + f(P_w)} + \left(1 - S_{gr} - S_{wr} \right) \frac{\phi c \lambda P_e^\lambda}{\left(P_g - P_w \right)^{(1+\lambda)}} \right] \frac{\partial P_w}{\partial t}
$$
$$
+ \left[S_w \phi + S_w (\phi - 1) \rho_s K_L \frac{C_{max}}{(1 + K_L c)^2} \right] \frac{\partial c}{\partial t} - \nabla \cdot (S_w \phi D \nabla c) + \nabla \cdot \left(\frac{k_{rw} k}{\mu_w} \nabla P_w c \right) = 0 \tag{33}
$$

3.5. Model for Coupled Water–Gas–Chloride Transport

The model for coupled water–gas–chloride transport in unsaturated concrete consists of three parts: the flow model for the gaseous phase, the flow model for the liquid phase, and the convection–diffusion model for chloride ions, as shown in Figure 3a–c. This model accounts for

the effects of convection, diffusion, chemical adsorption, and capillary action and reflects on the coupling effects between gas–liquid flows and solute transport in unsaturated porous media. The "gas phase term" represents the influence of the gas phase on the solute.

Figure 3. Water–gas–chloride coupling transport model in unsaturated concrete.

4. Model Calculations and Validation

4.1. Calculation Scheme

(1) Numerical model

The geometrical dimensions of the numerical model were 100×100 mm. The left boundary was subjected to chloride corrosion, whereas the remaining boundaries were non-seepage boundaries. Point A was slightly above the central line and was 5 mm from the left boundary, as shown in Figure 4.
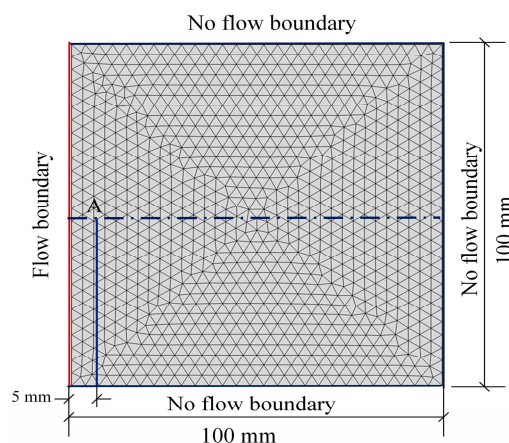

Figure 4. Numerical calculation model.

(2) Configuration of boundary conditions

According to the fluctuation of the sea level in the tidal zone during 24 h, the variation of the chloride concentrations in the left boundary during a single cycle (24 h) was described using Equation (34), as shown in Figure 5a. The variation of the pressure was described using Equation (35), as shown in Figure 5b.
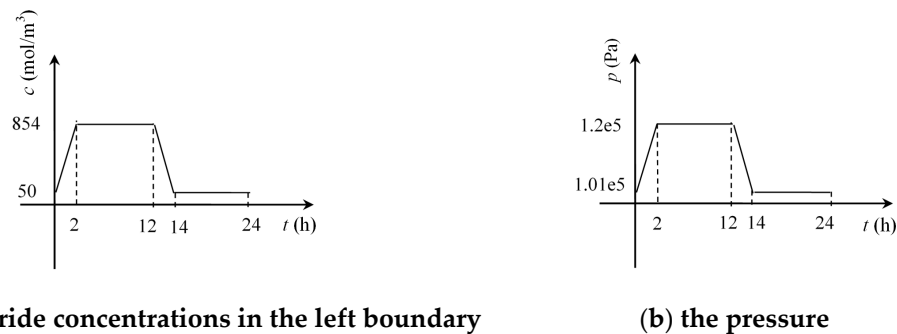

(a) the chloride concentrations in the left boundary　　　　**(b) the pressure**

Figure 5. Boundary conditions.

In Equation (34), $n = 0, 1, 2, 3, \ldots$, t represents the time (s), and $c(t)$ denotes the concentration of chloride ions (mol/m^3):

$$c(t) = \begin{cases} 50 + \frac{804}{7200} \times (t - 86400 \times n) & 0 + 86400 \times n \le t < 7200 + 86400 \times n \\ 854 & 7200 + 86400 \times n \le t < 43200 + 86400 \times n \\ 854 - \frac{804}{7200} \times (t - 43200 - 86400 \times n) & 43200 + 86400 \times n \le t < 50400 + 86400 \times n \\ 50 & 50400 + 86400 \times n \le t < 86400 + 86400 \times n \end{cases} \quad (34)$$

$$p(t) = \begin{cases} 1.01e5 + \frac{0.19e5}{7200} \times (t - 86400 \times n) & 0 + 86400 \times n \le t < 7200 + 86400 \times n \\ 1.2e5 & 7200 + 86400 \times n \le t < 43200 + 86400 \times n \\ 1.2e5 - \frac{0.19e5}{7200} \times (t - 43200 - 86400 \times n) & 43200 + 86400 \times n \le t < 50400 + 86400 \times n \\ 1.01e5 & 50400 + 86400 \times n \le t < 86400 + 86400 \times n \end{cases} \quad (35)$$

In Equation (35), $n = 0, 1, 2, 3 \ldots$, t is the time (s), and $p(t)$ is the boundary pressure (Pa).

(3) Scheme of the numerical calculation

Numerical simulation scheme is shown in Table 5.

Table 5. Numerical simulation scheme.

Scheme	Parameter	
	ϕ_0 %	D_0 ($\times 10^{-12}$ m^2/s)
Scheme 1	3.49	2.235
Scheme 2	3.83	2.974
Scheme 3	4.71	3.793

(4) Parameters for the numerical calculation

Since it is very difficult to obtain solutions for coupled models with complicated boundary conditions, the model in this work was further simplified prior to the calculations. For example, ϕ, ρ_w, and D were set to constant values, based on the values described by previous studies (Table 6).

Table 6. Numerical simulation parameters.

Parameter	Value
Initial porosity ϕ_0/%	ϕ_0
Pore deformation coefficient α/(1/Pa)	1e-6
Pressure compressibility β_p /(1/Pa)	5e-8
Concentration compressibility β_c/ (m^3/mol)	1e-5
Water permeability k_w/(m^2)	1e-15
Langmuir adsorption constant K_L/(m^3/mol)	0.001
Langmuir maximum adsorbing capacity C_{max}/(mol/m^3)	100
Initial concentration C_0/(mol/L)	50
Solution density ρ_w/(kg/m^3)	1025
Gas density ρ_g/(kg/m^3)	1.23
Concrete density ρ_c/(kg/m^3)	2450
Chloride diffusion coefficient D_0/(m^2/s)	D_0
Liquid dynamic viscosity u_w/(Pa·s)	0.00101
Gas dynamic viscosity u_g/(Pa·s)	0.00085
Liquid initial pressure P_0/(Pa)	1.01e5
Liquid initial saturation S_{wr}/%	30
Gas initial saturation S_{gr}/%	70
Concrete permeability K_0/(m^2)	1e-14

4.2. Results and Analysis

(1) Variation of model parameters

In this section, the variation of parameters such as saturation, permeability, relative permeability, and chloride ion concentration during the first cycle were analyzed.

(1-1) Variations in saturation

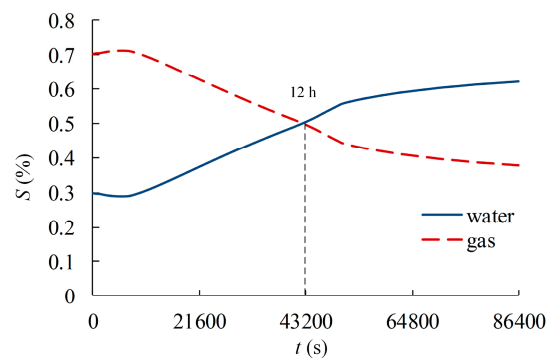Figure 6 shows the variation of saturation, *S*, at Point A with time, *t*, during the first cycle.

Figure 6. The change curves of saturation, *S*, with time, *t*.

It can be observed that the chlorides were transmitted into the concrete within the first 12 h, thus increasing the solution saturation and decreasing the gas saturation. During the period between the 12th and the 24th hour, surface water evaporation led to a decrease in the solution saturation and an increase in the gas saturation.

(1-2) Variations in fluid permeability

Figure 7 shows the variation of the ratio between the solution permeability, k_w, and the initial solution permeability, k_{w0}, (k_w/k_{w0}) at Point A with time, *t*, during the first cycle.
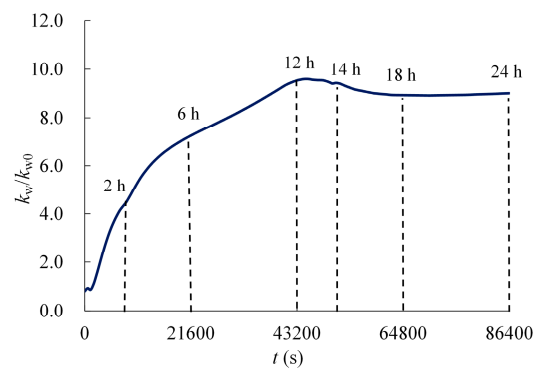
Figure 7. The change curves of the solution permeability ratio, k_w/k_{w0}, with time, t.

At t = 12 h, k_w reached its maximum value, which was 10 times the value of k_{w0}; at t = 24 h, the value of k_w was 9 times that of k_{w0}. Further, the curve can be divided into six segments. When t = 0–2 h, the solution permeability ratio, k_w/k_{w0}, grew at its most rapid rate, at 1.50/h. This suggests that the solution rapidly entered the concrete during this period. When t = 2–6 h, the rate of k_w/k_{w0} growth decreased to 0.75/h. When t = 2–12 h, k_w/k_{w0} continued to increase, but with a lower, stabilized rate of 0.33/h. When t = 12–14 h, k_w/k_{w0} began to decrease slowly, indicating that the solution on the concrete surface had begun to evaporate. When t = 14–18 h, k_w/k_{w0} continued to decrease, and eventually stabilized, such that k_w/k_{w0} = 9.0 when t = 18 h. When t = 18–24 h, the solution permeability ratio, k_w/k_{w0}, was maintained at a steady value.

(1-3) Variations in relative permeability

Figure 8 shows the variation of the relative permeability of the solution, k_{rw}, and the relative permeability of the gas phase, k_{rg}, at point A with time, t, during the first cycle.
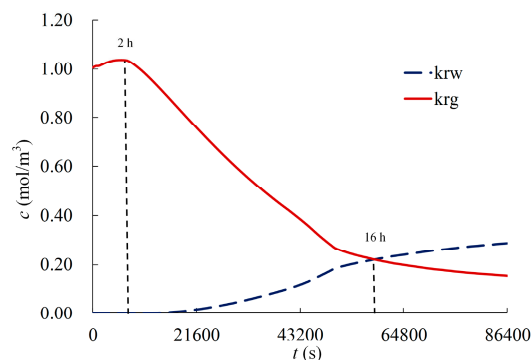

Figure 8. The change curves of gas and liquid relative permeability, k_{rg} and k_{rw}, respectively, with time, t.

When t = 0–2 h, k_{rg} increased, whereas k_{rw} was nearly zero. Most of the pores in the concrete were initially stable and filled with gas. When the boundary liquid pressure increased, the gas within the concrete changed from a stable state to a flow-dominated state. Consequently, the relative permeability of the gas increased slightly. Since the solution did not reach Point A, k_{rw} was zero. When t = 2–16 h, k_{rw} increased slowly and k_{rg} declined rapidly. When t = 16 h, k_{rw} = k_{rg}, indicating that most of the pores in the concrete were filled with water. When t = 12–24 h, k_{rw} continued to increase, albeit quite slowly, whereas k_{rg} continued to decrease slowly.

(1-4) Variations in chloride concentration within 24 h.

Figure 9 illustrates the variation of chloride concentrations, c, with depth, l, on the central line during the first cycle.
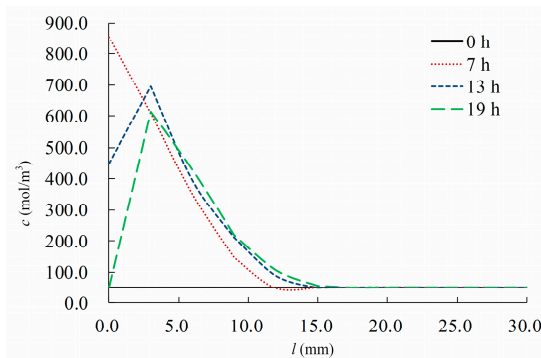
Figure 9. The change curves of chloride ion concentration, *c*, with depth, *l*.

At $t = 0$ h, the initial concentration, *c*, was 50 mol/m^3 at each of the points on the line. When $t = 0$–12 h, *c* decreased with an increase in *l*. When *l* reached a certain value, *c* reached its minimum value and remained steady. A peak value was not observed. When $t = 12$–24 h, *c* increased initially, and subsequently decreased with an increase in *l*. When *l* reached a certain value, the value of *c* reached a plateau. Therefore, there was a peak value of *c*. When the solution evaporated on the concrete surface, the chlorides dispersed and were transported internally and externally owing to the concentration gradients and capillary action. Consequently, a peak could be observed at a certain distance from the concrete surface.

(2) Variation of chloride concentrations

Numerical calculations were performed according to the schemes listed in Table 5. The initial porosities of each scheme were 3.49%, 3.83%, and 4.71%. The molar concentrations were converted to mass concentration to facilitate the experimental validation of the numerical results. The conversion formula is

$$c = \frac{c_1 M_{CL} \phi}{\rho_s} \tag{36}$$

where c_1 is the molar concentration of chloride ions, M_{CL^-} is the molar mass of chloride ions, ϕ is the porosity, and ρ_s is the density of the concrete samples.

The results of the coupling model presented in this study were compared with the experimental data and fitted results of Fick's Second Law, as shown in Figure 10. Figure 10a–d correspond to the results at 30, 110, 190, and 270 days, respectively. In the figure, 'test' corresponds to the experimental value, 'Fick' corresponds to the result obtained using Fick's Second Law, and 'couple' corresponds to the results of the proposed model. The following conclusions were drawn from the analysis of the results.

The results of the coupling model proposed in this study were consistent with the experimental results, indicating that the model provides a reasonable description of chloride transport in concrete. Nonetheless, a few deviations were observed between the model and experimental results because the equations were highly nonlinear and the calculations attenuated some of these expressions. Furthermore, the model did not account for the heterogeneity of the concrete.

As the depth increased, the fits obtained by Fick's Second Law gradually became smaller than the experimental results and their final values approached zero. The results of the model proposed in this work are thus superior to those of Fick's Second Law, since the proposed model produced a closer approximation of the experimental values. Since Fick's Second Law only considers the diffusion of chlorides and ignores the effects associated with gaseous flows, water migration, capillary actions, etc., it cannot provide an accurate description of chloride transport processes. These deficiencies have been addressed in the model proposed in this work.
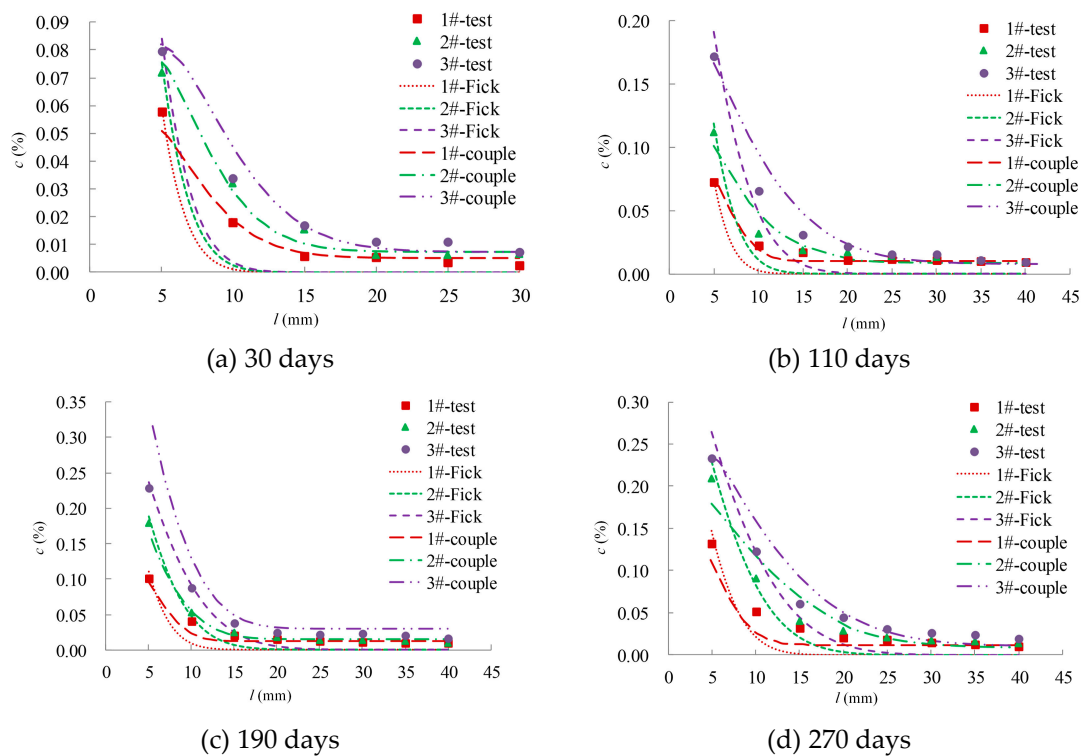
Figure 10. The comparison curves of chloride ion concentration, *c*, with depth, *l*.

5. Conclusions

(1) The porosities of concrete with 30% fly ash and 20% mineral powder were calculated under the action of three cyclic loading protocols (i.e., 50%, 65%, and 80% σ_c) and were 3.49%, 3.83%, and 4.71%, respectively.

(2) The chloride ion transport law of concrete was obtained by a salt spray corrosion test under the action of three cyclic loading protocols, and the average chloride ion diffusion coefficients of concrete were 2.235, 2.974, and 3.793×10^{-12} m^2/s, respectively, which were calculated by using Fick's Second Law.

(3) We have constructed a model for coupled water–gas–chloride transport in unsaturated concrete using gas flow models, liquid flow models, and solute convection–diffusion models. This model accounts for the effects of gas flows, water migration, convection–diffusion, and capillary actions and reflects on the coupling between gas–liquid flows and solute transport in unsaturated porous media.

(4) The coupled water–gas–chloride transport model was solved based on cyclic boundary conditions. The variations in parameters such as saturation, relative permeability, and chloride concentration during the first corrosion cycle were also analyzed. Through calculations performed on concretes with different initial porosities, this study has determined that the chloride concentrations calculated using the proposed model are consistent with the experimental results and are therefore superior to those obtained using Fick's Second Law.

Author Contributions: R.L. conceived and designed the experiments. X.M. and B.L. contributed to the theoretical calculation and numerical simulation parts of the work and composed the paper manuscript. H.Y. and L.Z. analyzed the data. All of the authors contributed to the writing of the paper.

References

1. Lv, J.F.; Tab, Z.J.; Ba, H.J. Micro-structure and performance analysis of marine concrete after extended exposure to marine environment. *J. China Univ. Min. Technol.* **2010**, *39*, 530–531.
2. Rita, B.F. Electrochemical sensors for monitoring the corrosion conditions of reinforced concrete structures: A review. *Appl. Sci.* **2017**, *7*, 1157.
3. Geng, J.; Easterbrook, D.; Liu, Q.F.; Li, L.Y. Effect of carbonation on release of bound chlorides in chloride contaminated concrete. *Mag. Concr. Res.* **2015**, *68*, 353–363. [CrossRef]
4. Yu, B.; Ning, C.; Li, B. Probabilistic durability assessment of concrete structures in marine environments: Reliability and sensitivity analysis. *China Ocean Eng.* **2017**, *31*, 63–73. [CrossRef]
5. Dai, H.J.; Wang, F.C.; Wu, Y.H.; Nan, F. Durability of concrete used for oil-platform in tidal zone. *J. Building Mater.* **2000**, *3*, 135–141.
6. Li, B.; Yin, H.G.; Mao, X.B.; Li, Y.; Zhang, L.Y.; Liu, R.X.; Qiu, P.T. Macroscopic and microscopic fracture features of concrete used in coal mine under chlorine salt erosion. *Int. J. Min. Sci. Technol.* **2016**, *26*, 455–459. [CrossRef]
7. Jin, W.L.; Zhang, Y.; Lu, Z.Y. Mechanism and mathematic modeling of chloride permeation in concrete under unsaturated state. *J. Chin. Ceram. Soc.* **2008**, *36*, 1362–1369.
8. Jin, W.L.; Jin, L.B.; Yan, Y.D.; Yao, C.J. Field inspection on chloride ion-intrusion effect of seawater in dry-wet cycling zone of concrete structures. *J. Hydraul. Eng.* **2009**, *40*, 364–365.
9. Zhang, Q.Z.; Gu, X.L.; Zhang, W.P.; Huang, Q.H. Model on capillary pressure saturation relationship for concrete. *J. Tong Ji Univ. Nat. Sci.* **2012**, *40*, 1753–1755.
10. Pan, Z.C.; Chen, A.R. Numerical simulation of chloride transportation process in unsaturated concrete. *J. Tong Ji Univ. Nat. Sci.* **2011**, *39*, 314–315.
11. Yan, Y.D.; Jin, W.L.; Wang, H.L.; Lu, C.H. Chloride transport in cracked concrete under wet-dry cycling condition. *J. Tong Ji Univ. Nat. Sci.* **2013**, *44*, 2060–2062.
12. Li, C.Q.; Li, K.F. Chloride ion transport in cover concrete under drying-wetting cycles: Theory, experiment and modeling. *J. Chin. Ceram. Soc.* **2010**, *38*, 581–582.
13. Li, C.Q.; Li, K.F. Moisture transport in cover concrete under drying-wetting cycles: Theory, experiment and modeling. *J. Chin. Ceram. Soc.* **2010**, *38*, 1151–1153.
14. Polder, B.P.; Peelen, W.H.A. Characterisation of chloride transport and reinforcement corrosion in concrete under cyclic wetting and drying by electrical resistivity. *Cem. Concr. Compos.* **2002**, *24*, 427–435. [CrossRef]
15. Thiery, M. Modelisation du sechage des betons: Analyse des differents modes de transfert hydrique. *Revue Européenne de Génie Civil* **2007**, *11*, 541–578. [CrossRef]
16. Ma, D.; Cai, X.; Li, Q.; Duan, H.Y. In-situ and numerical investigation of groundwater inrush hazard from grouted karst collapse pillar in longwall mining. *Water* **2018**, *10*, 1187. [CrossRef]
17. Li, K.F.; Li, C.Q.; Chen, Z.Y. Influential depth of moisture transport in concrete subject to drying-wetting cycles. *Cem. Concr. Compos.* **2009**, *31*, 693–698. [CrossRef]
18. Ma, D.; Duan, H.Y.; Liu, J.F.; Li, X.B.; Zhou, Z.L. The role of gangue on the mitigation of mining-induced hazards and environmental pollution: An experimental investigation. *Sci. Total Environ.* **2019**. [CrossRef]
19. Zanden, A.; Taher, A.; Arends, T. Modelling of water and chloride transport in concrete during yearly wetting/drying cycles. *Constr. Build. Mater.* **2015**, *81*, 120–123. [CrossRef]
20. Zhao, Y.X.; Chen, C.; Gao, X.J.; Jin, W.L. Seasonal variation of surface chloride ion content and chloride diffusion coefficient in a concrete doc. *Adv. Struct. Eng.* **2013**, *16*, 395–403. [CrossRef]
21. Zhou, Z.L.; Cai, X.; Ma, D.; Du, X.; Chen, L.; Wang, H.; Zang, H. Water saturation effects on dynamic fracture behavior of sandstone. *Int. J. Rock Mech. Min. Sci.* **2019**, *114*, 46–61. [CrossRef]
22. Wang, L.C.; Wang, J.Z. Mesoscale simulation of chloride diffusion in concrete subjected to flexural loading. *Adv. Struct. Eng.* **2014**, *17*, 561–571. [CrossRef]
23. Bourbatache, K.; Millet, O.; Aït-Mokhtar, A. Ionic transfer in charged porous media. Periodic homogenization and parametric study on 2D microstructures. *Int. J. Heat Mass Transf.* **2012**, *55*, 5979–5991. [CrossRef]

24. Ma, D.; Duan, H.Y.; Cai, X.; Li, Z.; Li, Q.; Zhang, Q. A global optimization-based method for the prediction of water inrush hazard from mining floor. *Water* **2018**, *10*, 1618. [CrossRef]
25. Wu, Y.; Liu, J.S.; Elsworth, D. Dual Poroelastic Response of coal Seam to CO_2 Injection. *Int. J. Greenh. Gas Control* **2010**, *4*, 668–678. [CrossRef]
26. Ma, D.; Rezania, M.; Yu, H.-S.; Bai, H.-B. Variations of hydraulic properties of granular sandstones during water inrush: Effect of small particle migration. *Eng. Geol.* **2017**, *217*, 61–70. [CrossRef]
27. Chilingar, G.V. Relationship between porosity, permeability, and grain size distribution of sands and sandstones. *Dev. Sedimentol.* **1964**, *1*, 71–74.
28. Zhou, Z.; Cai, X.; Ma, D.; Chen, L.; Wang, S.; Tan, L. Dynamic tensile properties of sandstone subjected to wetting and drying cycles. *Constr. Build. Mater.* **2018**, *182*, 215–232. [CrossRef]
29. Ma, D.; Cai, X.; Zhou, Z.L.; Li, X.B. Experimental investigation on hydraulic properties of granular sandstone and mudstone mixtures. *Geofluids* **2018**, *2018*, 9216578. [CrossRef]
30. Ge, Y.F. *Fine Numerical Simulation and Experimental Study of Chloride Corrosion of Self-Compacting Concrete*; School of Civil Engineering Southeast University: Nanjing, China, 2017; pp. 3–4.